

A Model-Driven Deep Neural Network for MRI Reconstruction with Unknown Sampling Pattern

Lina Sun, Hong Wang, Qi Xie, Yefeng Zheng, *Fellow, IEEE*, and Deyu Meng, *Member, IEEE*

Abstract—Against magnetic resonance imaging (MRI) reconstruction task, current deep learning based methods have achieved promising performance. Nevertheless, most of them are confronted with two main problems: 1) For most of current MRI reconstruction methods, the down-sampling pattern is generally preset and known in advance, which makes it hard to flexibly handle the complicated real scenario where the training data and the testing data are obtained under different sampling settings, thus constraining the model generalization capability. 2) They have not fully incorporated the physical imaging mechanism between the down-sampling pattern estimation and high-resolution MRI reconstruction into deep network design for this specific task. To alleviate these issues, in this paper, we propose a model-driven MRI reconstruction network with unknown sampling pattern, called MXNet. Specifically, based on the MRI physical imaging process, we first jointly optimize the down-sampling pattern and the high-resolution MRI reconstruction. Then based on the proposed optimization algorithm and the deep unfolding technique, we correspondingly construct the deep network where the physical imaging mechanism for MRI reconstruction is fully embedded into the entire learning process. Based on different settings between training data and testing data, including consistent and inconsistent down-sampling patterns, extensive experiments comprehensively substantiate the effectiveness of our proposed MXNet in detail reconstruction as well as its fine generality. Code is available at <https://github.com/sunliyangna0705/MXNet>.

Index Terms—MRI reconstruction, physical imaging mechanism, down-sampling pattern, generalization ability

I. INTRODUCTION

MAGNETIC resonance imaging (MRI) aims to adopt magnetic fields and computer-generated radio waves to produce detailed images of internal organs and tissues [1]. As a commonly-adopted medical imaging technology, it possesses specific merits such as non-invasiveness, high soft tissue contrast and multi-directional acquisition, and thus plays an important role in disease diagnosis. Considering MRI scanning

L. Sun and Q. Xie are with the School of Mathematics and Statistics, Xi'an Jiaotong University, Xi'an 710049, China. (e-mail: {linasun, xie.qi}@mail.xjtu.edu.cn).

H. Wang and Y. Zheng are with Jarvis Research Center, Tencent YouTu Lab, Shenzhen, China. (e-mail: {hazelhwang, yefengzheng}@tencent.com).

D. Meng is with the School of Mathematics and Statistics, Xi'an Jiaotong University, Xi'an 710049, China, and also with the Macau Institute of Systems Engineering, Macau University of Science and Technology, Taipa, Macau (e-mail: dymeng@mail.xjtu.edu.cn).

L. Sun and H. Wang equally contributed to this work.

is time-consuming that causes motion artifacts and discomfort to patients, how to achieve the fast MRI with favorable image quality is an important and meaningful problem [2].

Specifically, for scanned objects, MR images are obtained by inverse Fourier transform on the frequency domain k-space data collected from the MR scanner, and high-resolution MR images can be obtained by fully sampling the k-space data. To speed up the data acquisition process for single coil MR images, the widely-adopted method is to down-sample the k-space data. Such a degradation process can be written as [3]:

$$\mathbf{Y} = \mathbf{M} \odot \mathbf{F}\mathbf{X} + \boldsymbol{\varepsilon}, \quad (1)$$

where $\mathbf{X} \in \mathbb{C}^{H \times W}$ is the to-be-reconstructed MR image; \mathbf{F} is the Fourier transform operator; $\mathbf{M} \in \mathbb{R}^{H \times W}$ is a binary point-wise down-sampling matrix (mask) which delineates the sampling pattern executed in the k-space domain; specifically, $M_{ij} \in \{0, 1\}, i = 1, 2, \dots, H, j = 1, 2, \dots, W$; $\mathbf{Y} \in \mathbb{C}^{H \times W}$ is the under-sampled k-space data; \odot represents the dot product; $\boldsymbol{\varepsilon} \sim \mathcal{N}(0, \sigma^2 \mathbf{I})$ denotes the random Gaussian noise with noise level σ . Actually, in the process of MRI reconstruction, the down-sampling pattern matrix \mathbf{M} may be vary or unknown. Obviously, to reconstruct an image from under-sampled one is an NP-hard problem, which violates the Nyquist sampling criterion [4].

With the rapid development of deep learning, researchers have proposed diverse approaches to dealing with the fast MRI reconstruction task. These approaches can be broadly categorized into two types: data-driven and model-driven methods. Specifically, the former aims to utilize a large amount of training data to automatically learn the mapping function from under-sampled data to fully-sampled data, typically using k-space data or MR images. This is achieved through a variety of network architectures, including U-Net [5], generative adversarial network [6], ResNet [7], and CasCade-Net [8]. Although achieving promising performance, most of these methods are generally heuristically constructed based on off-the-shelf network blocks without fully considering the physical degradation mechanism in Eq. (1). To alleviate this issue, the model-driven research line for fast MRI reconstruction has emerged, which mainly focuses on integrating the physical imaging constraint into network designs via the deep unfolding technique [9] [10] [11]. Some excellent works have been proposed, such as ADMMCS-Net [12], convolution dealiasing network [13], variational network [14] [15], model-based deep learning (MoDL) [10], and neural proximal gradient descent [16]. Attributed to the involved optimization-

inspired unrolling design scheme, these model-driven methods generally have a clearer working mechanism than the purely data-driven fast MRI reconstruction methods. However, they are still confronted with a limitation, that is, the sampling pattern M in Eq. (1) is needed to be known and fed into networks as input. Such a non-blind operator is not well suited for real applications where the accurate down-sampling pattern for MR images is extremely hard to obtain in advance. This pre-defined setting would cause model drift and impair the reconstruction performance when the training phase and the testing phase have inconsistent degradation models with different down-sampling patterns M [17].

Recently, some researchers have tried to reconstruct the high-resolution MR image X with an unknown sampling pattern M [18]–[21]. For example, in LOUPE [18], the authors have assumed each point as an independent Bernoulli random variable with learnable distribution parameters on the full-solution k-space grid called probabilistic mask, and simultaneously optimize the sampling patterns M and the high-resolution MR image X . The drawback of this approach is the large number of trainable parameters and the learned sampling pattern is generic with respect to the training set (population-adaptive) rather than being adaptive to each individual object's characteristics. J-MoDL [19] assumes the sampling locations to be continuous variables and relies on an algorithm-dependent strategy to search for the best sampling pattern. Very recently, in [21] the authors have constructed an adaptive sampler via UNet, which can flexibly and dynamically generate the sampling pattern for each input MR image based on the limited low-frequency information from different scanned objects. Although the above methods try to handle the MRI reconstruction task in a blind manner, some issues still remain: 1) The learning of the down-sampling pattern M is heuristic, and it cannot finely reflect the degradation process underlying the acquired under-sampled measure Y , leading to the limited performance improvement; 2) The physical mechanism in Eq. (1) has not been fully embedded into network design for the joint optimization of M and X .

Against the aforementioned issues, in this paper, we fully consider the physical degradation model in Eq. (1) and propose a model-driven deep neural network with an unknown sampling pattern, called MXNet. Specifically, our contributions can be summarized as follows:

(1) **Model-Driven Joint Optimization of M and X .** Based on the physical degradation process Eq. (1), we construct the optimization model for the joint reconstruction of down-sampling pattern M and MR image X . We adopt the variable splitting technique [22] and the proximal gradient technique [23] to derive the optimization algorithm which alternately updates the unknown variables M and X . It is worth mentioning that our proposed model can be easily degraded to the non-blind case where the sampling pattern M is known.

(2) **Clear Network Design.** Based on the proposed optimization algorithm, we correspondingly construct the entire network framework by iterative unfolding every optimization step into the network connection into deep network operations. As shown in Fig. 1, the proposed MXNet mainly consists

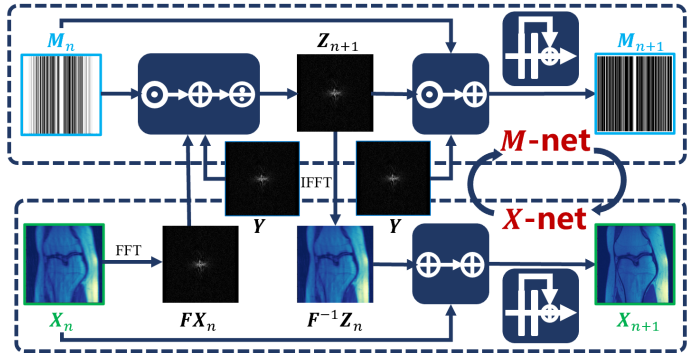


Fig. 1. Illustration of the proposed MXNet where the down-sampling mask M and the MR image X are jointly optimized based on the physical degradation model in Eq. (1).

of two sub-networks with clear connections to achieve the joint learning of the sampling pattern M and the MR image X . As observed, the mutual optimization of M and X always proceeds under the guidance of the physical model (1). Compared to the existing heuristic usage of M , which usually directly concatenating it with MR image [19], our design is in much clearer physical interpretability. Such a clear network design facilitates general readers to understand the working mechanism of MXNet by visualizing the model components extracted at every stage, as validated in Sec. V-C.

(3) **Fine Generality.** Based on different experimental settings, including consistent and inconsistent training-testing sampling patterns, we comprehensively validate the effectiveness of our proposed MXNet as well as its fine model generalization, as compared to current representative state-of-the-art MRI reconstruction methods. Attributed to the physics-driven adaptive design, our method can always extract rational down-sampling masks and then promote the full MRI recovery, showing obvious superiority in alleviating the model drift issue.

II. MRI RECONSTRUCTION MODEL

For the fast MRI reconstruction task, we first construct the optimization model for the joint recovery of down-sampling pattern M and MR image X and then derive the corresponding optimization algorithm.

A. Model Formulation

As in Eq. (1), given the under-sampled measure Y , our goal is to estimate the MR image X with unknown sampling pattern M . Mathematically, this can be formulated into the following optimization problem:

$$\min_{M, X} \|M \odot FX - Y\|_F^2 + \lambda_1 \mathcal{R}_1(M) + \lambda_2 \mathcal{R}_2(X), \quad (2)$$

where $M_{ij} \in \{0, 1\}$; λ_1 and λ_2 denote trade-off regularization parameters; $\|\cdot\|_F$ is the Frobenius norm. The first item in Eq. (2) reflects the physical generation mechanism of accelerated reconstruction of MR images, which provides explicit guidance in the iterative updating process of M and X . $\mathcal{R}_1(\cdot)$ and $\mathcal{R}_2(\cdot)$ represent the regularization terms and deliver the prior information of X and M , respectively.

To address the problem, we first introduce constraints for M , i.e., $(1 - M) \odot Y = 0$. This reflects the fact that when

$M_{ij} = 0$, $Y_{ij} = 0$ and when $Y_{ij} \neq 0$, $M_{ij} = 1$. Besides, we introduce an auxiliary variable Z , satisfied $Z = FX$. Then Eq. (2) can be transformed into the optimization problem:

$$\begin{aligned} & \min_{Z, M, X} \|M \odot Z - Y\|_F^2 + \lambda_1 \mathcal{R}_1(M) + \lambda_2 \mathcal{R}_2(X) \\ & \text{s.t. } Z - FX = 0, \quad (1 - M) \odot Y = 0, \end{aligned} \quad (3)$$

where we introduce the constraint $(1 - M) \odot Y = 0$ to indicate that the k-space data not sampled is 0. By converting the optimization problem (3) into an unconstrained optimization form, we can obtain that:

$$\begin{aligned} & \min_{Z, M, X} \|M \odot Z - Y\|_F^2 + \alpha \|FX - Z\|_F^2 \\ & + \beta \|(1 - M) \odot Y\|_F^2 + \lambda_1 \mathcal{R}_1(M) + \lambda_2 \mathcal{R}_2(X), \end{aligned} \quad (4)$$

where α and β denote penalty parameters. Similar to the existing model-driven methods, such as [24] [25], we rely on the flexible representation of CNN to automatically learn the implicit priors $\mathcal{R}_1(\cdot)$ and $\mathcal{R}_2(\cdot)$ from training data. More details are presented in Sec. III.

Especially, for the non-blind MRI reconstruction with the known down-sampling pattern M , Eq. (4) is simplified as:

$$\min_{Z, X} \|M \odot Z - Y\|_F^2 + \alpha \|FX - Z\|_F^2 + \lambda \mathcal{R}(X), \quad (5)$$

when $\alpha = +\infty$, Eq. (5) is corresponding to a standard compressed sensing model, which is the basis of many MRI reconstruction methods, such as [26]–[28]. As seen, they are the special case of our proposed reconstruction model.

B. Model Optimization

To solve the problem (4), we propose to adopt the proximal gradient method [23] to alternately update these unknown variables, including the auxiliary variable Z , down-sampling pattern M and the MR image X . Specifically, at the n -th iterative stage, the updating rules are derived as follows:

1) Updating Z : With X and M fixed, the auxiliary variable Z can be updated by solving the sub-problem about Z as:

$$\min_Z \|M_n \odot Z - Y\|_F^2 + \alpha \|FX_n - Z\|_F^2. \quad (6)$$

Clearly, we can directly derive the analytical solution as:

$$Z_{n+1} = \frac{\alpha F X_n + M_n \odot Y}{\alpha I + M_n^2}, \quad (7)$$

where I denotes the identity matrix and the division symbol represents an element-wise operation.

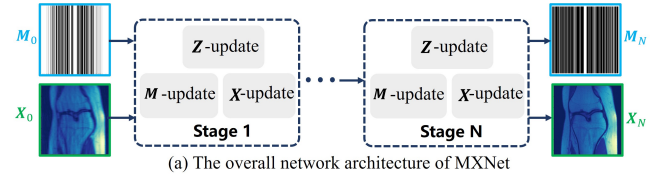
2) Updating M : With Z and X fixed, the down-sampling pattern M can be updated by solving the following problem:

$$\min_M \|M \odot Z_{n+1} - Y\|_F^2 + \beta \|(1 - M) \odot Y\|_F^2 + \lambda_1 \mathcal{R}_1(M). \quad (8)$$

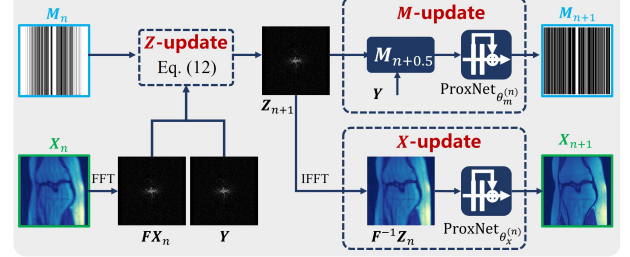
For the above formula, we can get the following formula by completing the square for the variable M :

$$\min_M \left\| \sqrt{Z_{n+1}^2 + \beta Y^2 + \omega} \odot \left(M - \frac{Z_{n+1} \odot Y + \beta Y^2}{Z_{n+1}^2 + \beta Y^2 + \omega} \right) \right\|_F^2 + \lambda_1 \mathcal{R}_1(M), \quad (9)$$

where ω is a very small number, in case of the denominator being 0. In experiments, we empirically set it to 1×10^{-6} .



(a) The overall network architecture of MXNet



(b) The network architecture at the n -th stage

Fig. 2. (a) The proposed MXNet includes N stages, and each stage contains three parts: Z -update, M -update, and X -update; (b) The network structure at the n -th stage based on Eqs. (15) (16) (17).

Furthermore, for the element-wise regularity, the Eq. (9) can be rewritten into the following form:

$$\min_M \left\| M - \frac{Z_{n+1} \odot Y + \beta Y^2}{Z_{n+1}^2 + \beta Y^2 + \omega} \right\|_F^2 + \frac{\lambda_1}{Z_{n+1}^2 + \beta Y^2 + \omega} \mathcal{R}_1(M), \quad (10)$$

With the coordinate descent algorithm [29], we can obtain the solution of Eq. (8) as:

$$M_{n+1} = \text{Prox}_{\Delta} \left(\frac{\beta Y^2 + Z_{n+1} \odot Y}{\beta Y^2 + Z_{n+1}^2 + \omega} \right), \quad (11)$$

where Prox_{Δ} represents the proximal operator, which is related to the regularization term $\Delta = \frac{\lambda_1}{Z_{n+1}^2 + \beta Y^2 + \omega}$. Similar to [24], we implement this operator via deep networks, as described in Sec. III.

3) Updating X : With Z and M fixed, the updating of X is accomplished by addressing the optimization sub-problem as:

$$\min_X \alpha \|FX - Z_{n+1}\|_F^2 + \lambda_2 \mathcal{R}_2(X). \quad (12)$$

Since F is a unitary transformation, Eq. (12) is equal to

$$\min_X \alpha \|X - F^{-1}Z_{n+1}\|_F^2 + \lambda_2 \mathcal{R}_2(X). \quad (13)$$

We can obtain the updating rule of X as:

$$X_{n+1} = \text{Prox}_{\lambda_2/\alpha} (F^{-1}Z_{n+1}), \quad (14)$$

where F^{-1} represents the inverse Fourier transform operator and $\text{Prox}_{\lambda_2/\alpha}(\cdot)$ represents the proximal operator, which is related to the regularization term $\mathcal{R}_2(\cdot)$.

As seen, for solving Eq. (4), the entire iterative process sequentially consists of Eqs. (7) (11) and (14), with simple operators, which makes it possible to unfold them into the corresponding network modules as analyzed below.

III. MODEL-DRIVEN MRI RECONSTRUCTION NETWORK

Motivated by the great success of the deep unfolding techniques in various tasks, including hyperspectral fusion [30] and CT metal artifact reduction [31], in the section, we aim to exploit this technique and carefully construct a model-driven MRI reconstruction framework by unfolding the iterative steps

(7)(11) and (14) into the corresponding network modules, called MXNet. As shown in Fig. 2 (a), the proposed MXNet is composed of N stages. For every stage, the network structure sequentially consists of Z -update, M -update, and X -update for accomplishing the iterative optimization of variables Z , M and X , respectively. Specifically, the corresponding operations are as follows:

$$Z\text{-update} : Z_{n+1} = \frac{\alpha F X_n + M_n \odot Y}{\alpha I + M_n^2}, \quad (15)$$

$$M\text{-update} : \begin{cases} M_{n+0.5} = \left(\frac{\beta Y^2 + Y \odot Z_{n+1}}{\beta Y^2 + Z_{n+1}^2 + \omega} \right) \\ M_{n+1} = \text{ProxNet}_{\theta_m^{(n)}}(M_{n+0.5}), \end{cases} \quad (16)$$

$$X\text{-update} : X_{n+1} = \text{ProxNet}_{\theta_x^{(n)}}(F^{-1}Z_{n+1}), \quad (17)$$

where $\text{ProxNet}_{\theta_m^{(n)}}$ and $\text{ProxNet}_{\theta_x^{(n)}}$ are shallow ResNets with the parameters $\theta_m^{(n)}$ and $\theta_x^{(n)}$ at the iterative stage n , which are adopted to automatically learn the proximal function Prox_{λ_1} and $\text{Prox}_{\lambda_2/\alpha}$, respectively. Similar to [24] [31], the two proximal network $\text{ProxNet}_{\theta_x^{(n)}}$ consists of two Resblocks, each formed by a sequence of Convolution+ReLU+Convolution+Skip Connection. $\text{ProxNet}_{\theta_m^{(n)}}$ has the same structure with $\text{ProxNet}_{\theta_x^{(n)}}$, while at the final iterative stage an extra sigmoid activation layer is adopted for constraining the optimized M to the range $[0, 1]$. Compared to the strict binary constraint $M_{ij} \in \{0, 1\}$, such a relaxation processing has been shown to facilitate a more effective information optimization in previous research [32].

According to Eqs. (15) (16) and (17), we can easily construct the network structure at each stage, as shown in Fig. 2 (b). All the parameters, including step size, penalty parameter and network parameters are learned in end-to-end. This is initialized Z_0 by Fourier transformer of under-sampled measure Y . Following this, according to formulas (16) (17), M_0 and X_0 are derived from Z_0 .

Remark: From the aforementioned analysis, it is easy to conclude that our proposed MXNet has its own specific merits: 1) In MXNet, the design of down-sampling pattern M is combined with the process of image reconstruction. M is learned in an almost explicit manner under the guidance of the physical imaging constraint, which has a better physical meaning and fully exploits the correlation to the actual under-sampled measure Y for refinement; 2) The inherent physical degradation process (1) is embedded in the design of the entire network framework, which finely guides the iterative updating of the sampling pattern M , the k-space data Z , and the MR image X ; 3) Such optimization-inspired network design makes our proposed MXNet have a clearer working mechanism and every network connection has its own physical meaning corresponding to the derived iterative step.

Training Loss. To train MXNet in an end-to-end manner, we adopt the following loss to supervise the joint reconstruction of the k-space data Z_n and the MR image X_n as:

$$\mathcal{L} = \sum_{n=1}^N \alpha_n \|X_n - X_{gt}\|_F^2 + \beta_n \|Z_n - Y_{gt}\|_F^2, \quad (18)$$

where α_n and β_n represent the weighting coefficients to balance different loss terms. In the experiment, for simplicity, we empirically set $\alpha_n = \beta_n = 0.1, n = 1, 2, \dots, N, \alpha_N = \beta_N = 1$. X_n and Z_n represent the recovered result in the image domain and frequency domain at the n -th iterative stage, respectively. X_{gt} denotes the ground truth MR image and Y_{gt} denotes the fully-sampled k-space frequency data which is obtained by the Fourier transformation of X_{gt} .

IV. EXPERIMENTAL DETAIL

Datasets. We comprehensively evaluate the effectiveness of the proposed MXNet based on two publicly available datasets, i.e., the Brain Dataset¹ and the Knee Dataset².

Specifically, the Brain Dataset [12] consists of 200 fully-sampled MR images with the 256×256 pixels collected from 10 volunteers. The imaging sequence parameters are given as: T1-weighted images: TE=2.29 ms, TR=1370 ms, FOV=220×220 mm², slice thickness=1 mm; and PD-weighted images: TE=10 ms, TR=1500 ms, FOV=220×220 mm, slice thickness=1 mm. According to the ratio 2:1:1, the 200 images are randomly split into training, validation, and testing, respectively. The single-coil Knee Dataset is from the NYU FastMRI Dataset [35] [36], and contains 34,742 fully-sampled MR images for training and 7,135 ones for testing which are acquired under the Coronal PD-weighted Protocol as: TE =27-32 ms, TR = 2750-3000 ms, FOV = 140×140 mm² and slice thickness = 3 mm. For every MR image, it is cropped to the central region of 320×320 pixels.

For each dataset, given the aforementioned fully-sampled MR image X_{gt} , following the publicly available simulation procedure³, we can generate the accelerated Cartesian down-sampling matrix M and then synthesize the corresponding under-sampled k-space data Y based on the degradation process in Eq. (1). More details about M and the noise level σ are described in the following experiments where we consider several different settings for comprehensive comparisons.

Implementation Details. Our proposed MXNet is implemented based on the PyTorch framework [37] with two NVIDIA Tesla V100 GPUs with 32G memory. The total number of iterative stages N is 10 and the ResBlocks in every proximal network is 2. Adam optimizer is utilized to train the network and the batch size is 1. For the Brain Dataset and Knee Dataset, the total numbers of training epochs are 1000 and 30, respectively. The initial learning rate is 0.0003 and it is multiplied by 0.5 at epochs [40, 80] for the Brain Dataset.

Comparison Baselines. We compare the proposed MXNet with different baselines, including traditional zero-filling methods [33], deep learning-based ADMMCS-Net [12], MoDL [10], and MD-Rec-Net [34] which are non-blind and need to take the simulation down-sampling mode M into deep networks as input. For a fair comparison, we also evaluate our proposed framework in the non-blind case, called XNet which corresponds to the problem (5) and can be easily constructed

¹<https://github.com/yangyan92/Deep-ADMM-Net>

²<https://fastmri.med.nyu.edu/>

³<https://github.com/facebookresearch/fastMRI>

TABLE I

(CONSISTENT TRAINING-TESTING CASE): THE AVERAGE PSNR (dB), SSIM(%) AND NRMSE(%) OF ALL COMPARISON METHODS ON BRAIN DATASET AND KNEE DATASET UNDER DIFFERENT DOWN-SAMPLING FACTORS AND NOISE LEVELS σ .

Method	Brain Dataset ($\sigma=0$)									Knee Dataset ($\sigma=0$)		
	$\times 4$			$\times 8$			$\times 10$			$\times 4$		
	PSNR↑	SSIM↑	NRMSE↓	PSNR↑	SSIM↑	NRMSE↓	PSNR↑	SSIM↑	NRMSE↓	PSNR↑	SSIM↑	NRMSE↓
Zero-Filling [33]	28.34	68.01	24.16	23.61	52.75	43.53	22.32	48.78	53.83	27.32	62.45	28.01
ADMMCS-Net [12]	37.15	88.96	7.89	25.91	62.91	25.21	24.21	58.58	29.55	—	—	—
MoDL [10]	36.24	86.78	9.36	26.81	63.38	28.23	25.81	60.93	32.44	29.34	66.44	22.64
MD-Rec-Net [34]	34.20	85.03	11.59	25.95	64.93	29.15	25.67	65.28	31.13	29.46	68.26	22.66
MXNet	37.74	90.43	7.79	29.56	71.21	20.28	29.07	69.77	21.61	30.82	68.27	19.77
XNet	37.95	91.25	7.60	29.69	71.17	19.96	28.97	69.37	21.83	30.78	68.28	19.84

Method	Brain Dataset ($\sigma=0.03$)									Knee Dataset ($\sigma=0.03$)		
	$\times 4$			$\times 8$			$\times 10$			$\times 4$		
	PSNR↑	SSIM↑	NRMSE↓	PSNR↑	SSIM↑	NRMSE↓	PSNR↑	SSIM↑	NRMSE↓	PSNR↑	SSIM↑	NRMSE↓
Zero-Filling [33]	25.95	48.49	32.74	22.64	35.36	50.33	21.58	32.87	60.13	22.92	61.02	48.03
ADMMCS-Net [12]	32.76	76.26	13.35	24.59	56.89	28.78	22.87	52.47	33.64	—	—	—
MoDL [10]	30.24	69.34	18.83	20.59	20.39	67.38	20.38	19.86	66.22	27.74	63.37	26.53
MD-Rec-Net [34]	31.30	<u>80.59</u>	15.62	25.98	66.00	49.05	25.83	66.04	32.43	29.85	<u>68.25</u>	21.70
MXNet	33.89	80.28	11.91	28.79	67.39	22.15	28.21	66.55	23.70	30.66	67.96	20.05
XNet	34.08	81.29	11.68	29.09	67.81	21.27	28.61	66.78	22.72	30.80	68.33	19.81

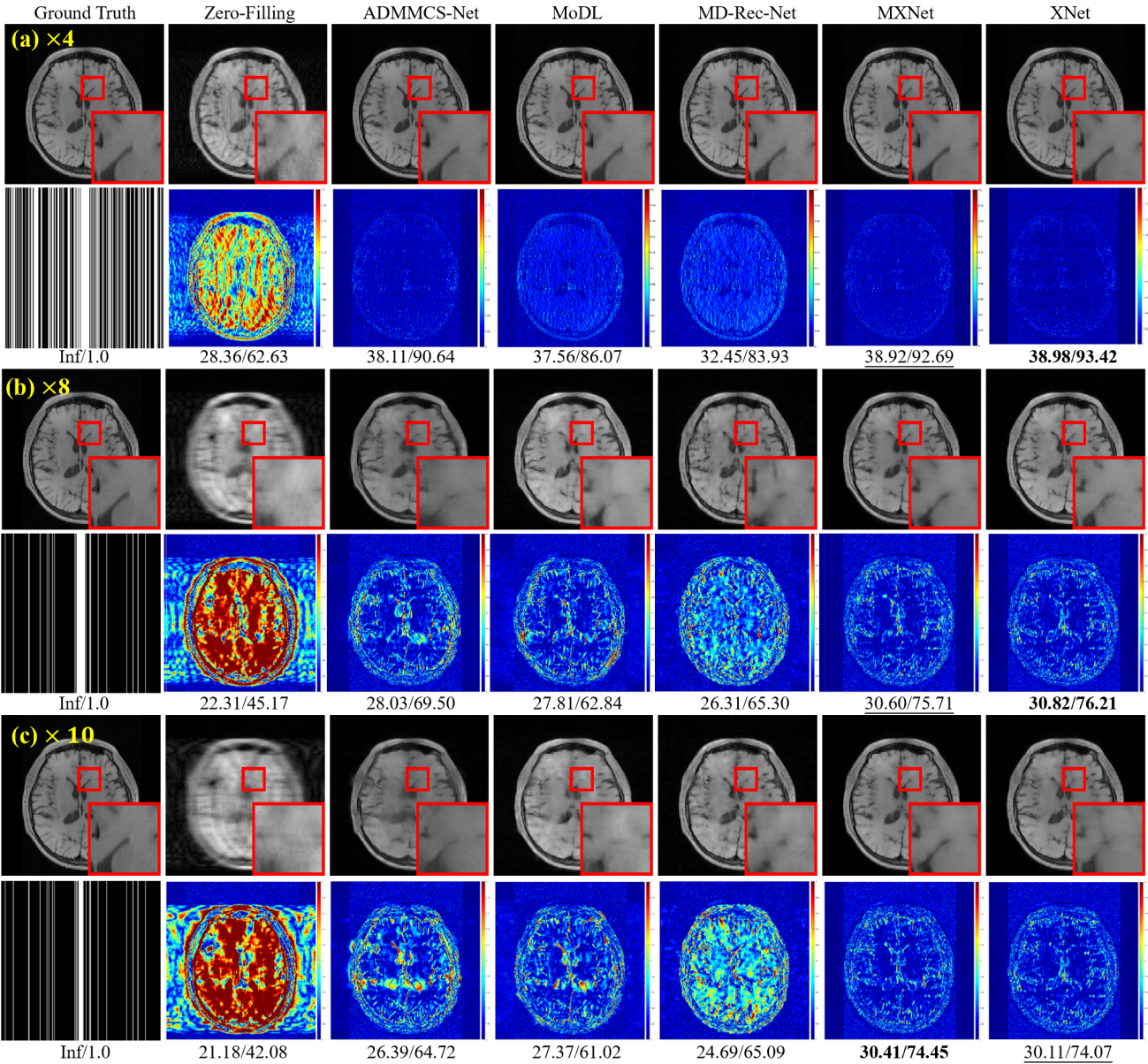


Fig. 3. (Consistent training-testing case): Comparison on the Brain Dataset under different down-sampling factors with the noise-free setting ($\sigma = 0$). Specifically, for every factor setting, the first row shows the reconstructed image and the second row represents the error maps between its reconstructed result and the ground truth. The first column of images is respectively a ground truth image and down-sampling pattern. PSNR/SSIM listed below for reference.

by removing the M -update in Fig. 1 where sampling mode M is known and we only need to estimate Z and X .

Performance Metrics. Following [14] [15] [18], we use the commonly-adopted metrics for the quantitative evaluation on the MR reconstruction performance, including peak signal-to-noise ratio (PSNR) [38], structural similarity (SSIM) [38] and normalized root mean square error (NRMSE) [12].

V. EXPERIMENTAL RESULTS

In this section, to comprehensively validate the effectiveness of our proposed methods, for the down-sampling pattern M and the noise level σ in the degradation process Eq. (1), we consider several experimental settings, including consistent training-testing cases and inconsistent training-testing cases.

A. Consistent Training-Testing Setting

In the consistent training-testing setting, for every dataset, we adopt the degradation process (1) with the same down-sampling pattern M to generate the training set and testing set. Here M is generated based on the $\times s$ accelerated Cartesian down-sampling setting where s is the down-sampling factor.

Quantitative Evaluation. Table I evaluates various methods across different down-sampling factors s ($s = 4, 8, 10$) for the Brain Dataset and only $s = 4$ for the Knee Dataset due to its larger size. Due to the time-consuming, we did not include ADMMCS-Net results for the Knee Dataset. The experiments of both datasets are executed on noise-free ($\sigma = 0$) and noisy setting ($\sigma = 0.03$).

It is clearly observed that: 1) Compared to other baselines, our proposed methods (*i.e.*, MXNet and XNet) consistently achieve higher PSNR and SSIM scores, and obtain lower NRMSE on the two benchmark datasets under different settings, *i.e.*, down-sampling factors and noise levels; 2) It is expected that compared to the noiseless case ($\sigma = 0$), the introduction of the random noise ($\sigma = 0.03$) adversely affects the accurate estimation of k-space data and almost all the comparison methods present a performance drop for MR reconstruction. However, even in this more challenging scenario, our proposed MXNet and XNet still achieve the competing performance. Especially, the blind MXNet is comparable to the non-blind XNet, showing the good robustness of the proposed down-sampling mask estimation; 3) Although the blind MXNet not preset the down-sampling mode as a known input, it always obtains a quite competitive reconstruction performance, which is only slightly inferior to the non-blind XNet. This finely substantiates the effectiveness and the rationality of the proposed deep unfolding framework. It is the explicit embedding of the physical imaging mechanism defined in Eq. (1) that helps MXNet optimize in a right direction, thus achieving the accurate extraction of the sampling pattern and then boosting the fine estimation of MR images.

Visual Evaluation. Fig. 3 presents the reconstruction results and the corresponding error maps as well as PSNR/SSIM on an image slice randomly selected from the Brain Dataset under different down-sampling factors in the noise-free case. As seen, the traditional Zero-Filling method contains severe artifacts. MoDL, ADMMCS-Net, and MD-Rec-Net blur image

details to some extent. In contrast, our proposed methods consistently achieve better image fidelity and obtain higher PSNR/SSIM scores under different down-sampling factors, and the corresponding error maps show fewer artifacts.

Fig. 4 presents the comparisons on noisy case for Brain Dataset. It is evident to see that deep learning based methods ADMMCS-Net, MoDL and MD-Rec-Net are more sensitive to noise and they cause obvious blurring effects. The noise consistently causes the restored MR images exhibit varying degrees of detail loss and smoothness. Nevertheless, from the comparisons on error maps, it is noticed that our proposed methods achieve better detail preservation, resulting in higher PSNR/SSIM scores. Similar trends can be observed on the Knee Dataset as shown in Fig. 5. More results are included in <https://sunliyangna0705.github.io/mx/>.

B. Inconsistent Training-Testing Setting

In clinical applications, to obtain a comprehensive and accurate representation of anatomy, multi-source MRI with different sampling protocols is usually adopted [39]. Motivated by this practical necessity, we further simulate a more complicated setting that for each fully-sampled MR image from either the training set or the testing set, the corresponding degraded k-space data is generated based on different $\times s$ accelerated Cartesian down-sampling patterns M for Eq. (1). Similar to Sec. V-A, for this inconsistent training-testing scenario, we also consider two different noise-level settings, *i.e.*, noise-free case with $\sigma = 0$, and noisy case with $\sigma = 0.03$.

Quantitative Evaluation. Table II lists the results of different comparison methods under this inconsistent training-testing setting with different noise levels. Compared with Table I where the training set and testing set have the same simulation process, it is evidently observed that facing such a more challenging cross-domain testing setting, the performance of almost all the comparing methods deteriorates dramatically, especially on the Brain Dataset. However, the performance of our proposed MXNet and XNet fluctuates less and shows strong generalization. It is worth mentioning that the blind MXNet is comparable even superior to the non-blind XNet. This is mainly attributed to the careful model-driven network design, which is helpful for rationally regularizing the mask learning and finely boosting the joint estimation of MR images, thus alleviating the cross-domain issue.

Visual Evaluation. Fig. 6 display the visual reconstruction of various methods on Brain Dataset with the noisy setting $\sigma = 0.03$. Fig. 7 shows that visual comparison on Knee Dataset $\times 4$ down-sampling setting under the noisy setting $\sigma = 0, 0.03$. As seen, our proposed MXNet accomplishes better reconstruction effect with higher structural fidelity under different down-sampling rates. For the noisy inconsistent training-testing setting, the existence of the simulation noise negatively impairs the MR image restoration. However, our proposed MXNet and XNet still perform competitively.

C. Model Verification

To fully validate the rationality of our proposed model-driven down-sampling mask learning, we provide the visu-

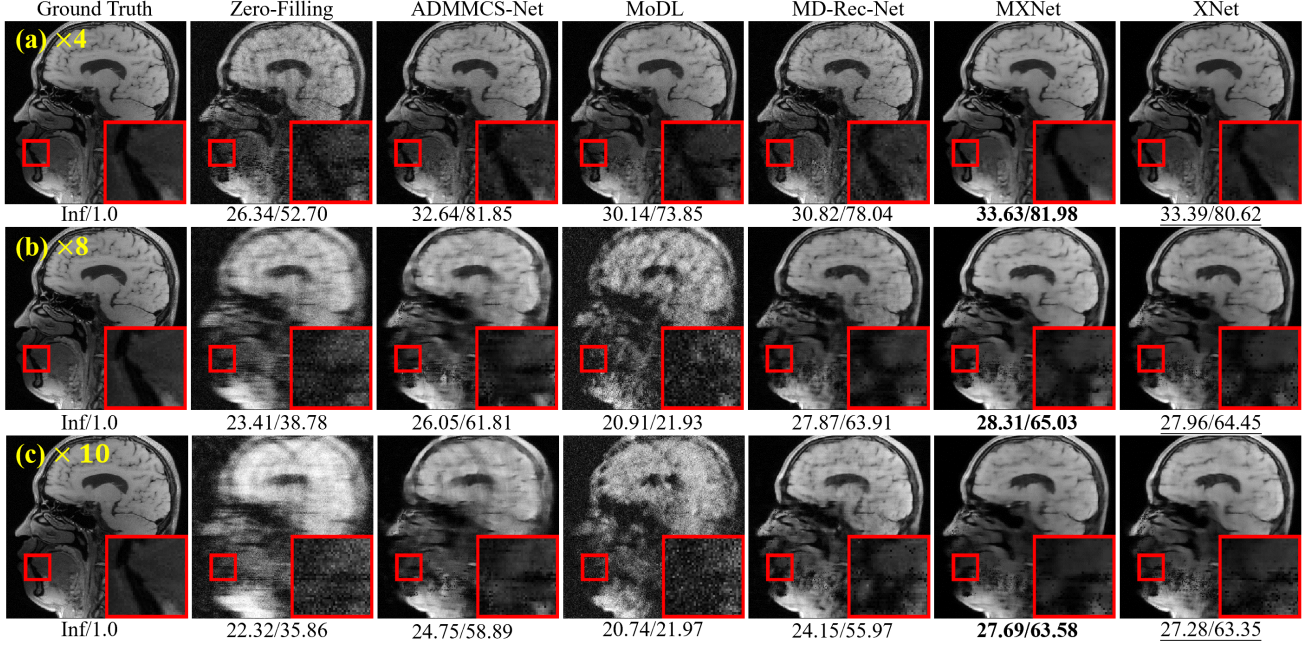


Fig. 4. (Consistent training-testing case): Comparison on Brain Dataset under different down-sampling factors with the noisy setting ($\sigma = 0.03$).

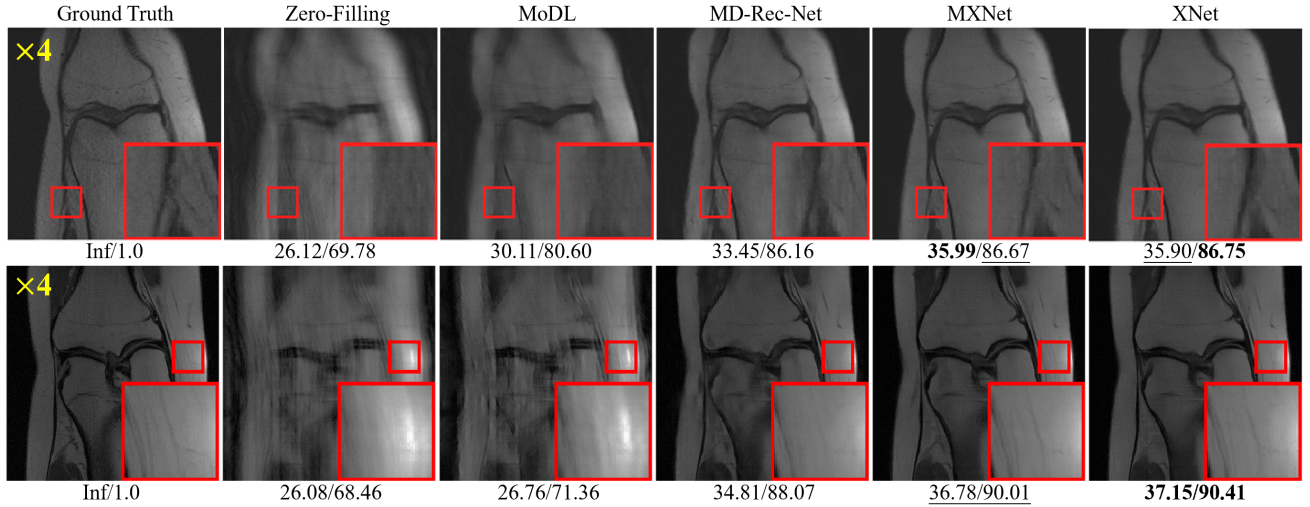


Fig. 5. (Consistent training-testing case): Comparison on Knee Dataset under $\times 4$ down-sampling factor with $\sigma = 0$ (top) and $\sigma = 0.03$ (bottom).

TABLE II

(INCONSISTENT TRAINING-TESTING CASE): THE AVERAGE PSNR (dB), SSIM(%) AND NRMSE(%) OF ALL COMPARISON METHODS ON THE BRAIN DATASET AND KNEE DATASET UNDER DIFFERENT DOWN-SAMPLING FACTORS AND NOISE LEVELS σ .

Method	Brain Dataset ($\sigma=0$)									Knee Dataset ($\sigma=0$)		
	$\times 4$			$\times 8$			$\times 10$			$\times 4$		
	PSNR↑	SSIM↑	NRMSE↓	PSNR↑	SSIM↑	NRMSE↓	PSNR↑	SSIM↑	NRMSE↓	PSNR↑	SSIM↑	NRMSE↓
Zero-Filling [33]	19.46	51.55	51.19	22.43	46.65	36.99	21.91	44.55	39.86	26.36	65.73	33.11
ADMMCS-Net [12]	34.58	85.14	11.10	24.53	60.03	28.95	22.51	54.42	33.63	—	—	—
MoDL [10]	32.46	84.40	12.52	25.14	59.71	34.26	24.18	58.34	38.80	29.78	65.74	21.59
MD-Rec-Net [34]	30.71	78.94	17.38	24.61	62.07	32.69	22.54	59.51	49.74	30.34	69.42	20.68
MXNet	36.18	89.11	9.49	28.09	68.49	23.77	27.29	66.18	26.03	31.58	68.83	18.49
XNet	36.06	89.01	9.57	28.40	68.71	22.94	27.35	66.02	26.01	31.56	68.85	18.51
Method	Brain Dataset ($\sigma=0.03$)									Knee Dataset ($\sigma=0.03$)		
	$\times 4$			$\times 8$			$\times 10$			$\times 4$		
	PSNR↑	SSIM↑	NRMSE↓	PSNR↑	SSIM↑	NRMSE↓	PSNR↑	SSIM↑	NRMSE↓	PSNR↑	SSIM↑	NRMSE↓
Zero-Filling [33]	19.56	39.16	52.86	21.65	31.26	42.27	21.23	30.32	45.01	29.48	65.37	22.15
ADMMCS-Net [12]	30.69	71.29	16.74	23.01	52.87	32.72	21.62	49.54	36.91	—	—	—
MoDL [10]	27.62	60.80	25.89	20.27	18.25	67.97	20.12	18.48	67.92	29.76	65.91	21.58
MD-Rec-Net [34]	30.57	75.83	17.77	24.04	60.79	52.15	23.41	60.14	35.19	30.68	69.29	20.11
MXNet	32.62	76.63	13.86	27.38	64.04	25.60	26.96	63.63	27.35	31.44	68.52	18.71
XNet	32.68	77.05	13.72	28.02	65.58	23.97	27.14	64.10	26.66	31.62	68.95	18.43

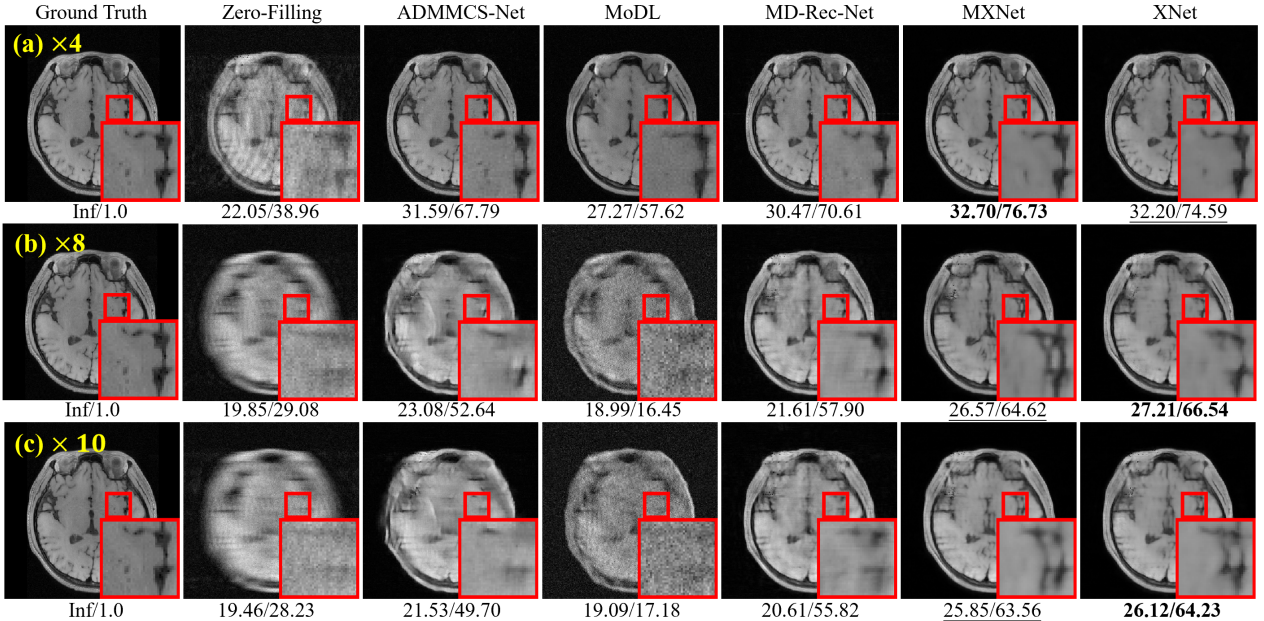


Fig. 6. (Inconsistent training-testing case): Comparison on Brain Dataset under different down-sampling factors with the noisy setting ($\sigma = 0.03$).

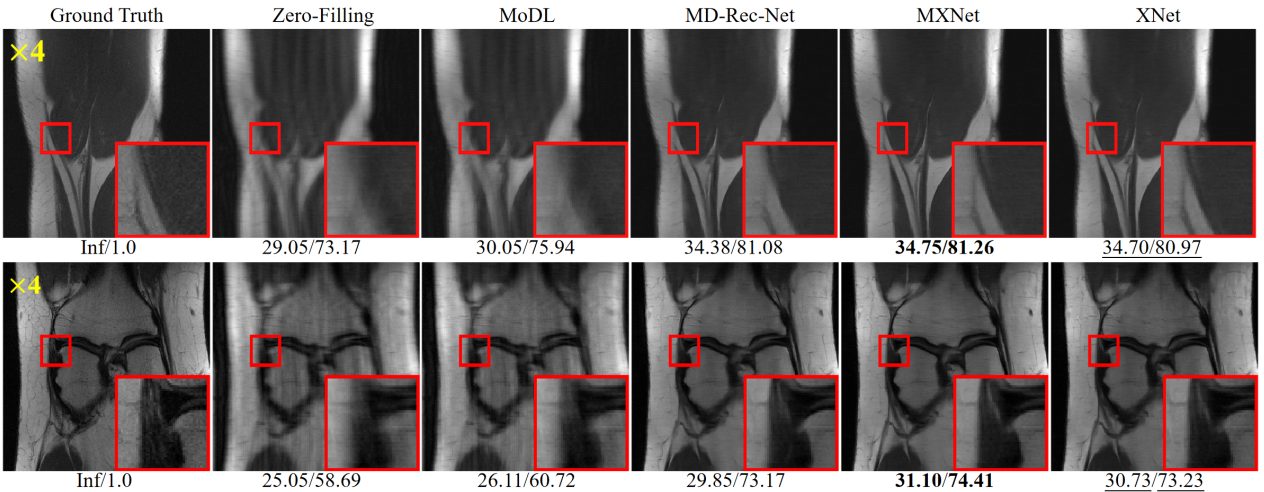


Fig. 7. (Inconsistent training-testing case): Comparison on Knee Dataset with $\sigma = 0$ (upper) and $\sigma = 0.03$ (lower).

TABLE III

AVERAGE PSNR (dB), SSIM(%) AND NRMSE(%) OF CXNET AND MXNET UNDER INCONSISTENT TRAINING-TESTING SETTING.

Methods	Brain Dataset ($\times 4$)			Knee Dataset ($\times 4$)		
	PSNR↑	SSIM↑	NRMSE↓	PSNR↑	SSIM↑	NRMSE↓
Inconsistent training-testing: noise level $\sigma = 0$						
CXNet	34.69	86.65	11.30	31.40	68.45	18.74
MXNet	36.18	89.11	9.49	31.58	68.83	18.49
Inconsistent training-testing: noise level $\sigma = 0.03$						
CXNet	31.88	74.21	15.09	31.41	68.45	18.75
MXNet	32.89	78.05	13.47	31.44	68.52	18.71

alization about the working mechanism underlying the proposed MXNet. Besides, for better evaluation, we also add the comparison with a degraded version, named as CXNet, where the proposed M -update is replaced by a conventional convolutional network. That is to say, for CXNet, without the iterative computation procedure derived in Eq. (16), the down-sampling mask M is directly estimated by feeding Z_n into the CNN network. The design of the CNN network is identical to ProxNet $_{\theta_m^{(n)}}^{(n)}$ of the M -update.

In Table III, the quantitative results of CXNet and MXNet are presented, particularly under the inconsistent training-

TABLE IV
EFFECT OF THE TOTAL STAGE NUMBER N ON THE PERFORMANCE OF THE PROPOSED MXNET ON BRAIN DATASET.

Stage N	PSNR↑	SSIM↑	NRMSE↓	Inference Time
$N = 2$	29.87	71.67	19.02	0.09s
$N = 4$	30.77	72.69	17.00	0.10s
$N = 6$	29.26	69.93	20.56	0.12s
$N = 8$	32.30	75.28	14.40	0.14s
$N = 10$	32.62	76.63	13.86	0.16s
$N = 12$	32.52	76.01	14.05	0.17s

testing setting described in Sec. V-B with $\times 4$ Cartesian sampling pattern. The comparison demonstrates that our MXNet consistently surpasses CXNet in performance under noise levels $\sigma = 0, 0.03$. This performance evaluation was conducted on both the Brain Dataset and Knee Dataset, reinforcing the effectiveness of MXNet in these varied contexts. Based on the Brain Dataset, Fig. 8 displays the iterative reconstruction processes of CXNet and MXNet under the inconsistent training-testing setting with noise level $\sigma = 0.03$. It is clearly observed that the down-sampling mask M learned from CXNet mainly occupies the middle low-frequency regions and then results in a relatively smooth reconstructed image. In contrast, the

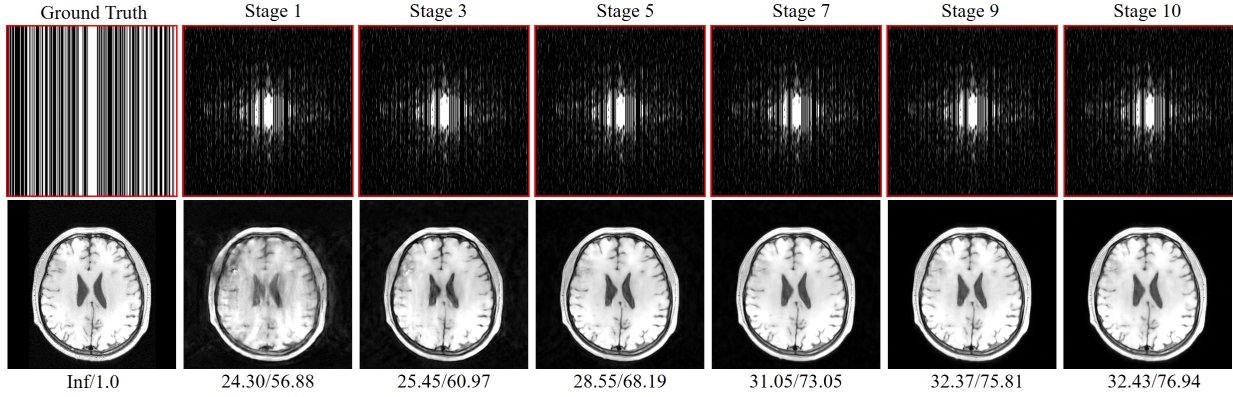
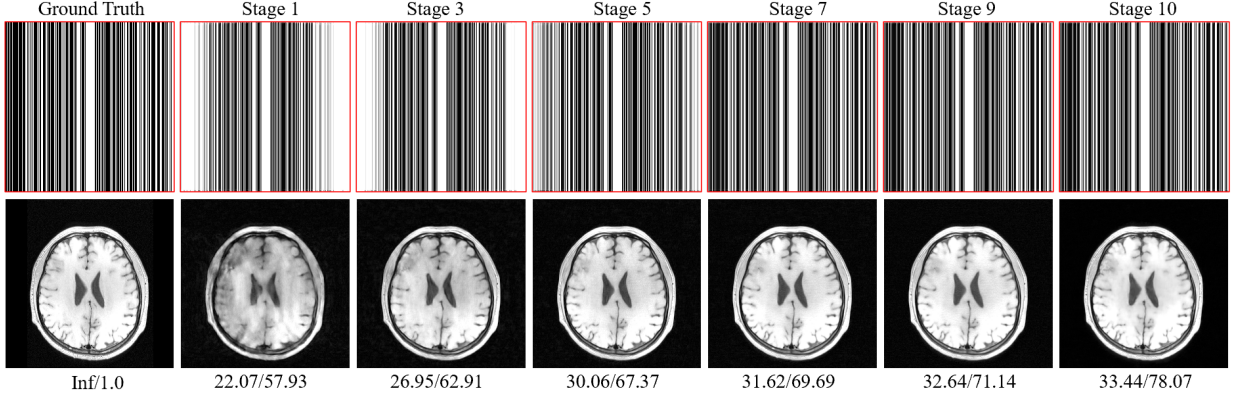
(a) Down-sampling pattern M_n and the corresponding MR image X_n reconstructed by CXNet at different stages.(b) Down-sampling pattern M_n and the corresponding MR image X_n reconstructed by MXNet at different stages.Fig. 8. The extracted down-sampling pattern M_n and the corresponding MR image X_n from CXNet and MXNet at different stages.

TABLE V

RESULTS OF OUR PROPOSED MXNET AND XNET ON BRAIN DATASET UNDER DIFFERENT PARAMETER SETTINGS FOR PROXNET $_{\theta_m}$ AND PROXNET $_{\theta_x}$ ACROSS DIFFERENT ITERATIVE STAGES.

Method	$\times 4$			$\times 8$			$\times 10$			Parameters
	PSNR↑	SSIM↑	NRMSE↓	PSNR↑	SSIM↑	NRMSE↓	PSNR↑	SSIM↑	NRMSE↓	
MXNet (Shared)	32.62	76.63	13.86	27.38	64.04	25.60	26.96	63.63	27.35	315.5k
MXNet (Unshared)	32.67	77.67	13.83	27.95	66.14	24.01	27.33	63.06	25.79	1,730.6k
XNet (Shared)	32.68	77.05	13.72	28.02	65.58	23.97	27.14	64.10	26.66	315.3k
XNet (Unshared)	32.69	77.75	13.85	28.04	66.28	23.96	27.44	63.91	25.63	1,729.0k

down-sampling mask extracted by M -update in the proposed MXNet is gradually improving and approaching the ground truth, which in turn enhances the image reconstruction quality achieved by the X -update module. Such favorable mutual promotion of M and X is inherently attributed to the rational physical imaging based model-driven network design.

D. Ablation Study

The Impact of the Number of Stages N . Based on the noisy inconsistent training-testing setting on Brain Dataset with $\times 4$ down-sampling as described in Sec. V-B, we investigate the impact of the number of iterative stages N on the performance of the proposed MXNet. As reported in Table IV, with varying N from 2 to 10, the reconstruction performance is generally improving at the cost of increasing inference time. Here the times is averagely computed on one image with 256×256 pixels based on an NVIDIA Tesla V100 GPU. Besides, when we increase N from 10 to 12, there is a slight decrease in performance. To strike a balance between network performance and inference time, we set N to 10 in all comparison experiments, as deeper network structures can hinder effective gradient propagation.

ProxNet $_{\theta_m^{(n)}}$ and ProxNet $_{\theta_x^{(n)}}$ across Different Stages. Here we study the proximal networks ProxNet $_{\theta_m^{(n)}}$ and ProxNet $_{\theta_x^{(n)}}$ by separately setting their involved network parameters $\theta_m^{(n)}$ and $\theta_x^{(n)}$ to be shared or unshared between different stages. Table V reports the results of MXNet and XNet on the Brain Dataset under the noisy inconsistent setting with different down-sampling factors. As observed, with the non-shared setting, both MXNet and XNet can generally achieve better reconstruction performance with higher PSNR/SSIM scores and lower NRMSE score, which outperforms the corresponding version with shared setting, respectively. However, such performance improvement comes at the expense of increased network parameters. Considering the performance and computation cost, in all experiments, we choose the parameter-shared setting for different iterative stages by default.

VI. CONCLUSION

In this paper, against the MR reconstruction task with unknown down-sampling pattern, we built the model-driven blind MR reconstruction network, called MXNet. Through model visualization, we validated the clear working mechanism underlying the proposed MXNet. Comprehensive experiments

conducted on different settings substantiated the superiority and robustness of our proposed method beyond the current representative MR reconstruction methods as well as its fine generalization capability in the cross-domain scenario. The proposed model-driven paradigm together with the careful designs for mask learning can be easily extended to the multi-coil imaging scene. In the future, we will further investigate the application potential of our proposed framework in more settings including different sampling protocols (*e.g.*, Cartesian or non-Cartesian sampling) and different sampling rates.

REFERENCES

- [1] C. M. Hyun, H. P. Kim, S. M. Lee, S. Lee, and J. K. Seo, “Deep learning for undersampled MRI reconstruction,” *Physics in Medicine & Biology*, vol. 63, no. 13, p. 135007, 2018.
- [2] G. Wang, J. C. Ye, K. Mueller, and J. A. Fessler, “Image reconstruction is a new frontier of machine learning,” *IEEE transactions on medical imaging*, vol. 37, no. 6, pp. 1289–1296, 2018.
- [3] A. Pal and Y. Rathin, “A review and experimental evaluation of deep learning methods for MRI reconstruction,” *The Journal of Machine Learning for Biomedical Imaging*, vol. 1, 2022.
- [4] C. E. Shannon, “Communication in the presence of noise,” *Proceedings of the IRE*, vol. 37, no. 1, pp. 10–21, 1949.
- [5] A. Aghabiglou and E. M. Eksioglu, “Projection-Based cascaded U-Net model for MR image reconstruction,” *Computer Methods and Programs in Biomedicine*, vol. 207, p. 106151, 2021.
- [6] G. Yang, S. Yu, H. Dong, G. Slabaugh, P. L. Dragotti, X. Ye, F. Liu, S. Arridge, J. Keegan, Y. Guo *et al.*, “DAGAN: deep de-aliasing generative adversarial networks for fast compressed sensing MRI reconstruction,” *IEEE transactions on medical imaging*, vol. 37, no. 6, pp. 1310–1321, 2017.
- [7] K. He, X. Zhang, S. Ren, and J. Sun, “Deep residual learning for image recognition,” in *Proceedings of the IEEE conference on computer vision and pattern recognition*, 2016, pp. 770–778.
- [8] J. Chlempner, J. Caballero, J. Hajnal, A. Price, and D. Rueckert, “A deep cascade of convolutional neural networks for dynamic MR image reconstruction,” *IEEE Transactions on Medical Imaging*, vol. 37, pp. 491–503, 2017.
- [9] A. Aghabiglou and E. M. Eksioglu, “Deep unfolding architecture for MRI reconstruction enhanced by adaptive noise maps,” *Biomedical Signal Processing and Control*, vol. 78, p. 104016, 2022.
- [10] H. K. Aggarwal, M. P. Mani, and M. Jacob, “MoDL: Model-based deep learning architecture for inverse problems,” *IEEE transactions on medical imaging*, vol. 38, no. 2, pp. 394–405, 2018.
- [11] J. A. Fessler, “Model-based image reconstruction for MRI,” *IEEE Signal Processing Magazine*, vol. 27, no. 4, pp. 81–89, 2010.
- [12] Y. Yang, J. Sun, H. Li, and Z. Xu, “ADMM-CSNet: A deep learning approach for image compressive sensing,” *IEEE transactions on pattern analysis and machine intelligence*, vol. 42, no. 3, pp. 521–538, 2018.
- [13] Y. Chen, T. Xiao, C. Li, Q. Liu, and S. Wang, “Model-based convolutional de-aliasing network learning for parallel MR imaging,” in *Medical Image Computing and Computer Assisted Intervention—MICCAI 2019: 22nd International Conference, Shenzhen, China, October 13–17, 2019, Proceedings, Part III 22*. Springer, 2019, pp. 30–38.
- [14] A. Sriram, J. Zbontar, T. Murrell, A. Defazio, C. L. Zitnick, N. Yakubova, F. Knoll, and P. Johnson, “End-to-end variational networks for accelerated MRI reconstruction,” in *Medical Image Computing and Computer Assisted Intervention—MICCAI 2020: 23rd International Conference, Lima, Peru, October 4–8, 2020, Proceedings, Part II 23*. Springer, 2020, pp. 64–73.
- [15] K. Hammernik, T. Klatzer, E. Kobler, M. P. Recht, D. K. Sodickson, T. Pock, and F. Knoll, “Learning a variational network for reconstruction of accelerated MRI data,” *Magnetic resonance in medicine*, vol. 79, no. 6, pp. 3055–3071, 2018.
- [16] M. Mardani, Q. Sun, D. Donoho, V. Papyan, H. Monajemi, S. Vasanawala, and J. Pauly, “Neural proximal gradient descent for compressive imaging,” *Advances in Neural Information Processing Systems*, vol. 31, 2018.
- [17] D. Gilton, G. Ongie, and R. Willett, “Model adaptation for inverse problems in imaging,” *IEEE Transactions on Computational Imaging*, vol. 7, pp. 661–674, 2021.
- [18] C. D. Bahadir, A. Q. Wang, A. V. Dalca, and M. R. Sabuncu, “Deep-learning-based optimization of the under-sampling pattern in MRI,” *IEEE Transactions on Computational Imaging*, vol. 6, pp. 1139–1152, 2020.
- [19] H. K. Aggarwal and M. Jacob, “J-MoDL: Joint model-based deep learning for optimized sampling and reconstruction,” *IEEE journal of selected topics in signal processing*, vol. 14, no. 6, pp. 1151–1162, 2020.
- [20] T. Weiss, O. Senouf, S. Vedula, O. Michailovich, M. Zibulevsky, and A. Bronstein, “PILOT: Physics-informed learned optimized trajectories for accelerated MRI,” *arXiv preprint arXiv:1909.05773*, 2019.
- [21] Z. Huang and S. Ravishankar, “Single-pass Object-adaptive data undersampling and reconstruction for MRI,” *IEEE Transactions on Computational Imaging*, vol. 8, pp. 333–345, 2022.
- [22] J. Geiser, *Iterative Splitting Methods for Differential Equations*. CRC Press, 2011.
- [23] I. Daubechies, M. Defrise, and C. De Mol, “An iterative thresholding algorithm for linear inverse problems with a sparsity constraint,” *Communications on Pure and Applied Mathematics: A Journal Issued by the Courant Institute of Mathematical Sciences*, vol. 57, no. 11, pp. 1413–1457, 2004.
- [24] J. Fu, H. Wang, Q. Xie, Q. Zhao, D. Meng, and Z. Xu, “KXNet: A model-driven deep neural network for blind super-resolution,” in *European Conference on Computer Vision*. Springer, 2022, pp. 235–253.
- [25] H. Wang, Q. Xie, Q. Zhao, and D. Meng, “A model-driven deep neural network for single image rain removal,” in *Proceedings of the IEEE/CVF conference on computer vision and pattern recognition*, 2020, pp. 3103–3112.
- [26] A. Majumdar, *Compressed Sensing for Magnetic Resonance Image Reconstruction*. Cambridge University Press, 2015.
- [27] M. Lustig, D. Donoho, and J. M. Pauly, “Sparse MRI: The application of compressed sensing for rapid MR imaging,” *Magnetic Resonance in Medicine: An Official Journal of the International Society for Magnetic Resonance in Medicine*, vol. 58, no. 6, pp. 1182–1195, 2007.
- [28] B. Deka and S. Datta, “Compressed Sensing Magnetic Resonance Image Reconstruction Algorithms,” *Springer series on bio-and neurosystems*, 2019.
- [29] S. J. Wright, “Coordinate descent algorithms,” *Mathematical programming*, vol. 151, no. 1, pp. 3–34, 2015.
- [30] Q. Xie, M. Zhou, Q. Zhao, Z. Xu, and D. Meng, “MHF-Net: An interpretable deep network for multispectral and hyperspectral image fusion,” *IEEE Transactions on Pattern Analysis and Machine Intelligence*, vol. 44, no. 3, pp. 1457–1473, 2020.
- [31] H. Wang, Y. Li, N. He, K. Ma, D. Meng, and Y. Zheng, “DICDNet: deep interpretable convolutional dictionary network for metal artifact reduction in CT images,” *IEEE Transactions on Medical Imaging*, vol. 41, no. 4, pp. 869–880, 2021.
- [32] T. Roubíček, *Relaxation in optimization theory and variational calculus*. Walter de Gruyter GmbH & Co KG, 2020, vol. 4.
- [33] M. A. Bernstein, S. B. Fain, and S. J. Riederer, “Effect of windowing and zero-filled reconstruction of MRI data on spatial resolution and acquisition strategy,” *Journal of magnetic resonance imaging: an official journal of the international society for magnetic resonance in medicine*, vol. 14, no. 3, pp. 270–280, 2001.
- [34] M. Ran, W. Xia, Y. Huang, Z. Lu, P. Bao, Y. Liu, H. Sun, J. Zhou, and Y. Zhang, “MD-Recon-Net: a parallel dual-domain convolutional neural network for compressed sensing MRI,” *IEEE Transactions on Radiation and Plasma Medical Sciences*, vol. 5, no. 1, pp. 120–135, 2020.
- [35] J. Zbontar, F. Knoll, A. Sriram, T. Murrell, Z. Huang, M. J. Muckley, A. Defazio, R. Stern, P. Johnson, M. Bruno *et al.*, “fastMRI: An open dataset and benchmarks for accelerated MRI,” *arXiv preprint arXiv:1811.08839*, 2018.
- [36] F. Knoll, T. Murrell, A. Sriram, N. Yakubova, J. Zbontar, M. Rabbat, A. Defazio, M. J. Muckley, D. K. Sodickson, C. L. Zitnick *et al.*, “Advancing machine learning for MR image reconstruction with an open competition: Overview of the 2019 fastMRI challenge,” *Magnetic resonance in medicine*, vol. 84, no. 6, pp. 3054–3070, 2020.
- [37] N. Ketkar, J. Moolayil, N. Ketkar, and J. Moolayil, “Introduction to pytorch,” *Deep Learning with Python: Learn Best Practices of Deep Learning Models with PyTorch*, pp. 27–91, 2021.
- [38] A. Hore and D. Ziou, “Image quality metrics: PSNR vs. SSIM,” in *2010 20th international conference on pattern recognition*. IEEE, 2010, pp. 2366–2369.
- [39] K. H. Kim, S. Seo, W. J. Do, H. M. Luu, and S. H. Park, “Varying undersampling directions for accelerating multiple acquisition magnetic resonance imaging,” *NMR in Biomedicine*, vol. 35, no. 4, p. e4572, 2022.